Production and decay of excited quasiprojectiles in peripheral and semiperipheral $^{35}Cl+^{197}Au$ reactions in Fermi energy domain

X. Qian,* L. Beaulieu,† X. Bai, Y. Larochelle,‡ B. Djerroud,§ R. Laforest,‖ L. Gingras, R. Roy, M. Samri,¶ and C. St-Pierre
Laboratoire de Physique Nucléaire, Département de Physique, Université Laval, Québec, Canada G1K 7P4

G. C. Ball,** D. R. Bowman,†† E. Hagberg, and D. Horn
AECL, Chalk River Laboratories, Chalk River, Ontario, Canada K0J 1J0

(Received 1 June 1998)

The peripheral and semiperipheral reactions in $^{35}Cl+^{197}Au$ have been studied at 30 and 43 MeV/nucleon. The nonequilibrium α and IMF components have been observed in the experiment. The fraction of nonequilibrium emission decreases with an increase in the atomic number of the projectilelike fragments but, for a given projectilelike fragment, it increases with the charge of the emitted particles. The characteristics of quasiprojectiles reconstructed from their decay products reveal several features reminiscent of damped reactions at lower bombarding energies. The atomic number and deflection angle of projectilelike fragments depend strongly on their kinetic energy or dissipated energy. At 30 MeV/nucleon, the experimental data can be explained by a deep inelastic transfer model. One-body dissipation is still the main mechanism for the energy and angular momentum dissipation. However, at 43 MeV/nucleon, deep inelastic transfer models can predict only the experimental tendency. Two-body dissipation plays a more important role at higher incident energies. The similarity observed in the decay product distributions, as a function of excitation energy, suggests that the excited quasiprojectiles formed in binary collisions might approach thermal equilibrium for both incident energies. The decay products have been analyzed with sequential-binary and simultaneous-disassembly statistical decay models. Both statistical models are able to provide good agreement with the experimental observables except for the mean kinetic energy of the products. [S0556-2813(99)05901-4]

PACS number(s): 25.70.Lm, 25.70.Mn

I. INTRODUCTION

The study of the production and decay of excited nuclear systems [1] and of the emission of intermediate-mass fragments (IMF's) [2,3] is of considerable current interest in heavy-ion reactions in the intermediate energy domain (10 MeV/nucleon $\leqslant E/A \leqslant$ 100 MeV/nucleon). Most of the past studies concentrated on the excited nuclear systems produced by complete or incomplete fusion in central collisions. Recently, experimental measurements showed that binary processes are still dominant at intermediate energies and they are an effective way to produce and study very hot nuclei [4–8]. They are expected to put more severe constraints on the theoretical approach than central collisions and some effects, such as compression and expansion modes, can be neglected. Critically excited quasiprojectiles (QP) with excitation energy as high as 8–10 MeV/nucleon have been observed experimentally [5–9]. The dynamical production of such a highly excited QP in binary collisions is not fully understood.

Heavy-ion collisions in the Fermi energy domain raise very complex problems in nuclear dynamics. At low energy, the Pauli principle inhibits nucleon-nucleon collisions. The reaction characteristic is one-body dissipation. The cross section between very heavy nuclei is dominated by deep inelastic collisions (DIC) [10]. Above the Fermi energy ($\approx$35 MeV/nucleon), the Pauli blocking is less and less effective. Nucleon-nucleon collisions are increasingly allowed, and eventually these collisions will dominate the reaction dynamics at high energies. Thus the strong competition between mean field and collision dynamics is expected to show up and the reaction mechanism may be transitional in this energy domain. Information on the competition or transition can be obtained from the study of energy and angular momentum dissipation in the collision. In fact, some authors [11,12] have studied the relative importance of the dissipative processes. A number of studies have shown that these still exist in the Fermi energy domain or have demonstrated at least partial damping at 60 MeV/nucleon [13–15]. Several experiments have been performed on heavy systems [16–18]; the binary cross sections are larger than for light systems because of the strong Coulomb repulsion. The importance of the dissipative process in the emission of fragments coming from excited QP and QT was also observed in the reaction of

*Present address: INRS-Télécommunications, Montréal, Québec, Canada.

†Present address: Lawrence Berkeley National Laboratory, Berkeley, CA 94720.

‡Present address: Indiana University Cyclotron Facility, Indiana University, Bloomington, IN 47408.

§Present address: Departement of Physics and Astronomy, McMaster University, Hamilton, Ontario, Canada L8S 4M1.

‖Present address: Cyclotron Institute, Texas A&M, College Station, TX 77843.

¶Present address: Département de Physique, Faculté des Sciences Université Ibn Toufail, Kénitra, Morocco.

**Present address: TRIUMF, 4004 Westbrook Mall, Vancouver, British Columbia, Canada V6T 2A3.

††Present address: Washington Aerial Measurements Operations, Bechtel Nevada, P.O. Box 380, Suitland, MD 20752.

$^{40}Ar+^{27}Al$, ^{58}Ni at 44 MeV/nucleon [19]. Other people [20,21] have discussed the incident energies of different systems at which the reaction mechanism changes from the low energy behavior to dominant transfer or abrasion mechanism for more violent collisions.

At lower bombarding energy and, hence, excitation energy, where evaporation of IMF's is strongly hindered by the large Coulomb barrier, the system deexcites mostly by emitting light charged particles (LCP's), γ-rays, and/or by fission. With increasing excitation energy, statistical IMF emission is expected to compete more efficiently with other deexcitation modes. Statistically emitted fragments have been observed in studies of the decay of highly excited compound nuclei formed in central collisions [22]. Recently, correlation measurements between IMF's and evaporation residues suggested that the deep inelastic process remains the dominant mechanism of IMF production for the $^{40}Ar+Ag$ reaction at 27–65 MeV/nucleon [13–15,23,24]. However, IMF multiplicity was found to exceed significantly the predictions of conventional statistical models in a number of experiments [25,26]. The discrepancy is explained as the evidence for the observation of necklike emission [18,27,28]. Moreover, there have also been observations of strong azimuthal angular correlations between energetic LCP's and IMF's as well as preferential emission of the LCP's in the same plane in which the IMF is emitted. These studies indicate that dynamical mechanisms play an important role in the production of IMF's [29–33].

Up to now, several models compete to describe peripheral or semiperipheral heavy-ion collisions: participant-spectator (PS) models, adapted from higher energies [34,35], deep inelastic transfer (DIT) models [36,37], and microscopic dynamical models [38–40]. Recent experiments show that the so-called projectile fragmentation, at the incident energy of 60 MeV/nucleon, is more like a low energy mechanism than a high energy one, as in the PS model [41]. The DIT model extended from lower energies has been successfully applied to reactions in the Fermi energy domain [37]. Microscopic transport equations, such as Boltzmann-Uehling-Uhlenbeck (BUU) equation, have been widely used to simulate the evolution of heavy-ion collisions in the intermediate energy domain. It is able to deal with a variety of processes ranging from complete or incomplete fusion to deep-inelastic reactions. BUU treats the initial nonequilibrium stage of the collision in reasonable details and should yield a good prediction for the preequilibrium nucleon emission and the production of highly excited QP's and quasitargets (QT's). However, the emission of IMF's is also not yet fully understood. For statistical IMF emission, there are two limiting scenarios. One is the sequential binary decay, a sequence of well-separated emissions from an equilibrated parent nucleus [42–44]. The other is a simultaneous breakup of the deexciting system into many fragments [35,45–48]. No dynamical models can explain the necklike or dynamical emission of IMF's. To shed light on the emission mechanism, one should measure various observables simultaneously and compare with the predictions of these models.

In a previous study [6], we demonstrated, by applying an event-by-event analysis, that it was possible to reconstruct kinematically the primary QP in peripheral collisions irrespective of final charged particle multiplicities. In this study, we present some results obtained on the asymmetric system $^{35}Cl+^{197}Au$ at 30 and 43 MeV/nucleon. In the present paper, we deal with similar topics but with a special emphasis on the nonequilibrium emission from dissipative processes and the comparison of the same system at two incident energies. It is organized as follows: after briefly describing the experimental procedure in Sec. II, we will present the experimental results in Sec. III. The nonequilibrium particle emissions are analyzed. The qualitative results for nonequilibrium, equilibrium and dissipative collision processes are also discussed. In Sec. IV, some theoretical models used to understand the collision mechanism are presented; the hybrid approach is established. The binary dissipative processes have been analyzed with BUU models. The reconstructed characteristics of excited QP's are compared with the prediction of DIT models. The observable distributions of decay products are also explained by a statistical decay model. Finally in Sec. V, results will be summarized and conclusions presented.

II. EXPERIMENTAL PROCEDURE

A beam of ^{35}Cl was accelerated to 30 and 43 MeV/nucleon with the Tandem Accelerator SuperConducting Cyclotron (TASCC) facility at Chalk River and was used to bombard a 2.1 mg/cm^2 thick gold target. The forward reaction products were detected by the CRL-Laval Array covering the polar angles from 3.0° to 46.8° with respect to the beam axis. The 80 detectors of the array were mounted in five concentric rings around the beam axis and covered nearly 100% of the solid angle between 6.8° and 46.8°. The first three rings are made of plastic phoswich detectors with detection thresholds of 7.5 MeV/nucleon for $Z=1$ and 2 to 22.8 MeV/nucleon for $Z=17$ particles. The two outer rings are composed of CsI(Tl) crystals for which isotopic resolution is achieved for $Z=1$ and 2 with a threshold around 2 MeV/nucleon as well as identification of $Z=3$ and 4 with a threshold of 5 MeV/nucleon. The most forward angles, 3.0° to 5.0°, are covered by three Si-CsI telescopes which provide charge identification with a detection threshold of 2(5) MeV/nucleon for $Z=2(17)$ particle. The complete setup consists of 83 detectors providing the granularity needed to study high-multiplicity events in peripheral collisions. More details about the detection apparatus, energy calibration and particle identification can be found in Refs. [49–51].

III. EXPERIMENTAL RESULTS AND DISCUSSION

A. Experimental results

1. Fragment charge distributions

The measured yield distributions of fragments with the largest charge Z_{max} in each event and the corresponding total detected charge Z_{tot} as a function of atomic number are displayed in Fig. 1 for the four angular regions covered by the telescopes and phoswich detectors. The Z_{tot} distributions of two incident energies have been normalized at $Z_{tot}=9$ for comparison. The strong correlation between Z_{tot} and the atomic number of the primary QP, Z_{QP}, will be discussed in the next section. Although not all charged particles in the event are emitted from the statistical decay of the primary excited QP, some qualitative information about the excited

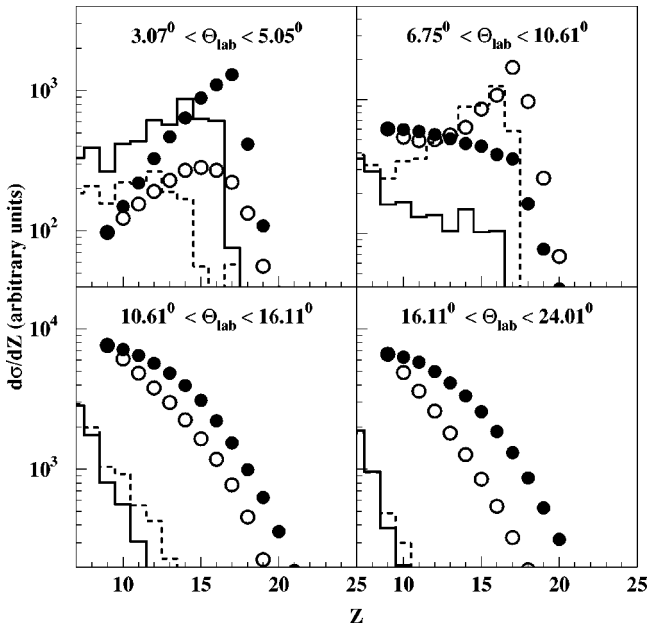

FIG. 1. The charge distributions of fragments with the largest charge Z_{max} in each event in four angular regions. The solid (dashed) line represents the detected Z_{max} distribution at 43 (30) MeV/nucleon. The full (open) circles are the total detected charge Z_{tot} distributions, in which the Z_{max} fragments are emitted in the indicated angular regions at 43 (30) MeV/nucleon.

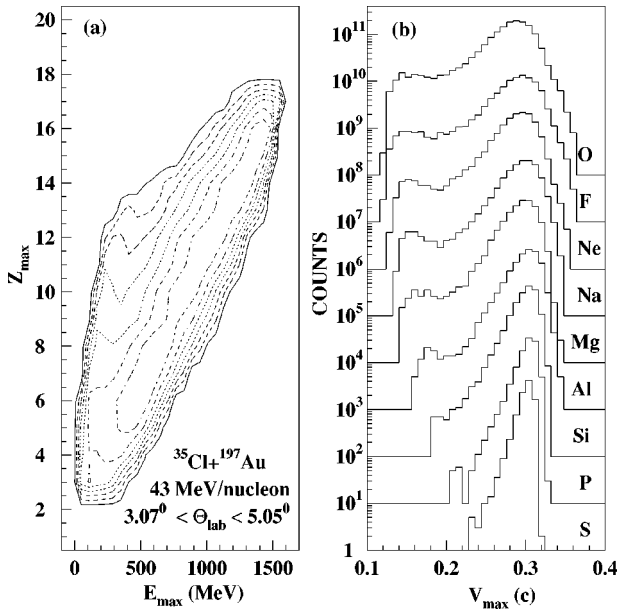

FIG. 2. Yield of fragments detected in the telescopes at $3.07° \leqslant \theta_{lab} \leqslant 5.05°$. (a) A logarithmic contour plots atomic number Z_{max} versus kinetic energy E_{max} of fragments. (b) The velocity distributions of different Z_{max} for $^{35}Cl + ^{197}Au$ reaction at 43 MeV/nucleon. For clarity, successive curves are multiplied by 10.

QP can still be obtained from the inclusive Z_{max} and Z_{tot} distributions. For 30 MeV/nucleon, the grazing angle 7.9° is in the angular region of the first ring phoswich detectors, $6.75° \leqslant \theta_{lab} \leqslant 10.61°$, so a very strong transfer or quasielastic peak can be seen in the Z_{tot} distribution at $Z_{tot} = 16$. For 43 MeV/nucleon, the grazing angle 6.11° is less than the minimum angle of the first ring phoswich detector, so there is no similar peak in the figure. The yield distributions at larger angles are very similar. The charge distribution decreases rapidly for $Z_{tot} \geqslant 17$ for both incident energies suggesting that the yields of fragments heavier than the projectile are suppressed. In the angular region of the telescopes, $3.07° \leqslant \theta_{lab} \leqslant 5.05°$, which is less than the grazing angle at both energies, the intensities of Z_{tot} distributions show the same trend for both experimental data, increasing first steadily with the increasing Z_{tot}, then decreasing from the maximum value. For the larger angular ranges $10.61° \leqslant \theta_{lab} \leqslant 16.11°$ and $16.11° \leqslant \theta_{lab} \leqslant 24.01°$, the Z_{tot} distributions are dominated by light fragments and show simply similar shapes with a near exponential falloff. The decrease is steeper for 30 MeV/nucleon than for 43 MeV/nucleon. The less different Z_{max} and Z_{tot} distributions near the grazing angle mean that the primary QP has less excitation energy. The difference between Z_{max} and Z_{tot} distributions increases considerably as the detected angle moves away from the grazing angle, where the primary QP's are highly excited.

2. Fragment velocity distributions

Figure 2(a) displays a logarithmic contour plot of the yield of the heaviest fragment Z_{max} versus its kinetic energy E_{max} measured by telescopes at $3.07° \leqslant \theta_{lab} \leqslant 5.05°$ for 43 MeV/nucleon. This figure shows a well-defined ridge. The cross section $d^2\sigma/dZdE$ along the ridge remains relatively constant down to $Z_{max} \approx 5$. The almost linear character of the correlation between Z_{max} and E_{max} suggests that the fragments have similar velocities. This result can be seen in Fig. 2(b), which shows the velocity distribution of different Z_{max} from 8 to 16 detected by the telescopes. As expected, one observes that the velocity distributions have a shape similar to those observed in other reactions in the Fermi energy domain: it has a maximum peak centered at a value somewhat below the beam velocity and an asymmetric shape with a longer tail toward small velocities. The distributions tend to approximately Gaussian shapes as the atomic number of the fragment decreases. The peak velocity of the spectra corresponds to about 80% of the beam velocity for large Z and to about 70% for small Z values. Considering the fragment charge and angular distributions, the main component can be attributed to the decay of the QP from transfer and dissipative processes. Both mechanisms are present in this transitional energy region.

Apart from the PLF major component, we find a second component from the evolution of velocity distributions in Fig. 2(b). The velocity distributions of that component are very broad, extending from the detection threshold to $0.2c \sim 0.25c$, about 70–75 % of beam velocity. The intensity of this second component decreases and its average velocity increases as the fragment charge Z_{max} increases. The existence of a second component can be confirmed in Fig. 2(a). At $Z_{max} \leqslant 7$, the two components merge together. For other systems at intermediate bombarding energies, similar distributions with two velocity components and the change in properties with the evolution of Z_{max} are also observed [15,52,53]. The second component was usually called intermediate-velocity fragments. Such fragments are of particular interest since their origin is not well known. There are significant differences in the explanation of their origin by

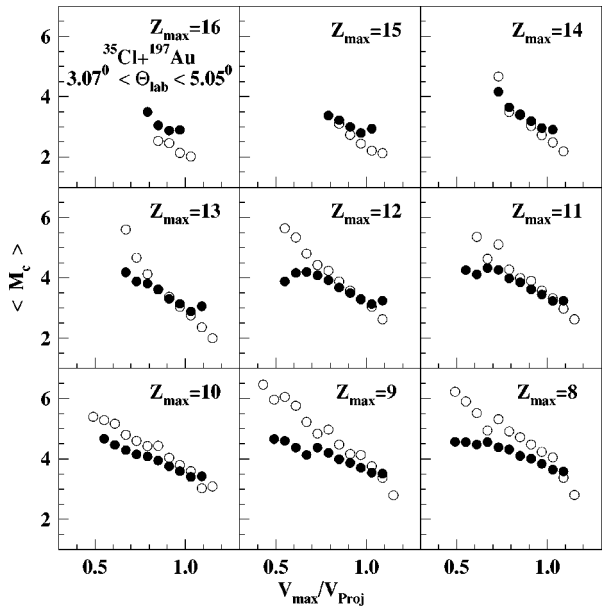

FIG. 3. Correlation between the velocity of PLF detected by telescopes and the total average charged particle multiplicity of all fragments and light charged particles (not corrected for detection efficiency). Each panel corresponds to a different PLF charge $Z_{\max}$ producted in the $^{35}Cl+^{197}Au$ reaction. The full and open circles represent the experimental data of 43 and 30 MeV/nucleon incident energies, respectively.

different models. In the participant-spectator model [34,35], it may be the remnants of a participant zone emitted by one of the two reaction partners or by the combined system. In the classical dynamical model [21] which is extended from low energy heavy-ion collisions, the fast component is explained as a positively deflected fragment with little dissipated energy and the lower velocity component as a negatively deflected fragment with a large dissipation. At 30 MeV/nucleon incident energy, a similar behavior is observed for the PLF's, but we cannot see the second component clearly. It may due to the relatively higher detection threshold for an incident energy of 30 MeV/nucleon compared to 43 MeV/nucleon.

3. The correlation between fragment velocity and charged particle multiplicities

Figure 3 shows the correlation between the velocity of the $Z_{\max}$ fragments detected by telescopes and the mean charged particle multiplicity M_C in each event for two incident energies. The velocities are normalized to the beam velocities. The data have not been corrected for the detection efficiency. Each panel represents a fragment $Z_{\max}$ from 8 to 16. For each fragment, the experimental data show a similar trend: the $\langle M_C \rangle$ decreases almost linearly with increasing $V_{\max}$. As discussed for the system $^{22}Ne+^{93}Rb$ at 35 MeV/nucleon [54] and $^{40}Ar+^{132}Xe$ at 44 MeV/nucleon [55], one expects that the strong correlation between charged particle multiplicity and impact parameter also exists in peripheral and semiperipheral collisions in the present system. The events with a larger multiplicity correspond to more violent collisions (smaller impact parameter). Some qualitative results can be deduced from this figure for both incident energies: for a given fragment, the lesser is the fragment velocity, the more violent the collision is; for a same fragment velocity, the more violent collisions result in lighter fragment emissions, and therefore, the lightest detected $Z_{\max}$ originates from a primary QP having the highest excitation energy. More highly excited QP's were produced at 43 MeV/nucleon than at 30 MeV/nucleon. Three observables, the charged particle multiplicity, fragment velocity and atomic number of the QP remnant are found to be strongly correlated.

B. Nonequilibrium emission

As described in the Introduction, it is possible to reconstruct the characteristics of the primary excited QP by applying an event-by-event analysis in the hypothesis of a binary process. However such a procedure is valid only if the particles are emitted statistically by the primary nuclei in thermal equilibrium. In fact, LCP's from preequilibrium and dynamical processes are both present. In order to determine the characteristics of the primary QP beyond the number and the energy of detected particles, one has to assess which fraction of these particles are really emitted from a nucleus in thermal equilibrium. The nonequilibrium particles should be eliminated at an acceptable level. In the following section, we present the characteristics of LCP's and IMF's emitted in coincidence with a massive PLF. For the remainder of the paper, PLF refers to fast forward moving fragments from the QP. The largest PLF (in Z) in each event is refer to as $Z_{\max}$.

1. Two-dimensional velocity distribution

One way widely used to obtain a global view of the particle emitter sources, which contribute to the emission of a given fragment with A_F or Z_F, is to plot a two-dimensional distribution of Galilean-invariant cross section $d^2\sigma/v_\perp dv_\perp dv_\parallel$ versus the particle velocity components parallel ($v_\parallel$) and perpendicular ($v_\perp$) to the emitter direction [56]. Figure 4 shows an illustration of typical Galilean-invariant velocity distributions of LCP's ($Z=1$ and 2) and IMF's ($Z=3$) as a function of $v_\parallel$ and $v_\perp$ in the emitter frame for the $^{35}Cl+^{197}Au$ system at 30 and 43 MeV/nucleon incident energies. The particles ($Z=1$, 2 and 3) are coincident with a $Z_{\max}=12$ fragment of velocity larger than 70% of beam velocity. In the analysis, the coincident particles and fragments were converted, event by event, into the frame of the emitter reconstructed from all detected particles in the event and the Z axis was chosen to lie along the final recoil velocity of the emitter. In the figure, a larger width in the mean velocity distribution is observed at 43 MeV/nucleon than at 30 MeV/nucleon, which suggests that more highly excited QP's are formed at 43 MeV/nucleon. A well-defined ''Coulomb ring'' shown in the velocity pattern would indicate that most of the particles are indeed emitted sequentially from the fully accelerated primary QP. However, there is a considerable number of particles located outside the rings as it can be seen in the figure for $Z=2$ and 3 particles. These particles, with only about half the beam velocity, cannot be explained as the products of a primary excited QP. They were referred to as ''non-QP equilibrium emitted particles'' [57]. They may come from the evaporation of an excited QT or/and other nonequilibrium processes. Although most evaporated particles from the primary QT have a low energy

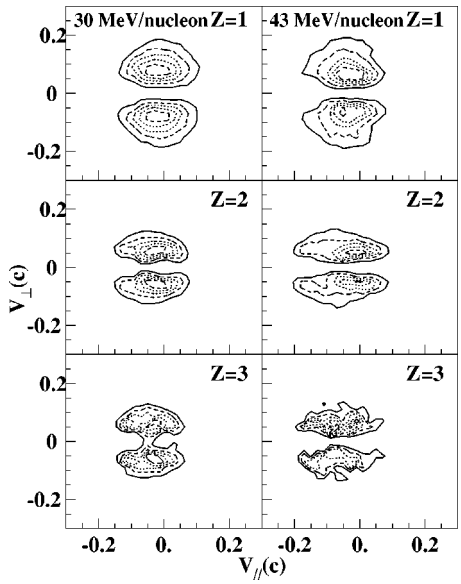

FIG. 4. Galilean-invariant velocity distributions of LCP's and IMF's as a function of $v_{\parallel}$ and $v_{\perp}$ in the emitter frame. The particles are in coincidence with a fragment of $Z_{\max}=12$ and velocity larger than 70% of beam velocity. The emitter frame is reconstructed from the total detected particles in the event.

and are eliminated by the energy thresholds of the detectors, such a contamination might still be present because of the relatively low thresholds of CsI detectors, at $0.07c$, $0.07c$, and $0.1c$ for $Z=1$, 2 and 3 particles respectively. However, in the following section, simulations show that the evaporation of a QT could not be strong enough to explain the observed yield of ''non-QP equilibrium emitted particles.'' Most of these particles should be accounted for from nonequilibrium processes. More of these particles are seen at 43 MeV/nucleon than at 30 MeV/nucleon.

A more obvious and systematic presence of nonequilibrium particles can be seen in Fig. 5, which shows the parallel

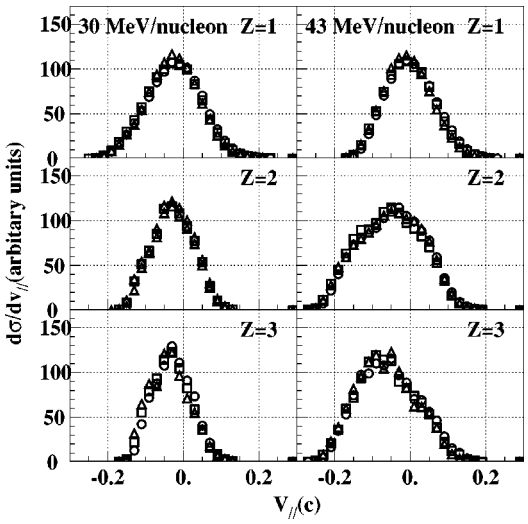

FIG. 5. The parallel velocity component ($v_{\parallel}$) of $Z=1$, 2, and 3 particles in the recoil direction of the emitter. The particles are coincident with a fragment with $Z_{\max}=9$, 10, or 11. The square, triangle and circle symbols represent the data of particles coincident with a fragment of $Z_{\max}=9$, 10, and 11, respectively.

velocity ($v_{\parallel}$) of particles $Z=1$, 2 and 3 coincident with fragments with $Z_{\max}=9$, 10 and 11. The direction of ($v_{\parallel}$) is along the recoil direction. Although the distortion caused by the detection system has not been taken into account, one can observe from the figure that the distributions are very asymmetric. The negative mean values show that more particles are emitted backward in the frame of the emitter. In fact, if a full 4π detector was used in the experiment and all particles emitted from a single source, the distributions should be symmetrical and centered at zero. For less than 4π geometry as in the present experiment, a forward emission should be enhanced because of the focusing at forward angles in the laboratory. The enhancement is stronger at 43 MeV/nucleon than at 30 MeV/nucleon. The discrepancies between experimental data and qualitative expectations suggest the presence of other complex emission processes. The velocity distributions obtained for particles of same Z are found to be independent of the coincident $Z_{\max}$.

2. The Monte Carlo simulations

To study the nonequilibrium emission more quantitatively, the possible distortion caused by the limitations of the experimental apparatus and recoil effects must be considered. A Monte Carlo simulation is performed to evaluate as closely as possible the experimental situation.

In the simulations, we focus on the events in which the heaviest fragment has been detected by the telescopes between 3.0° and 5.0°. The following hypotheses were made. (1) The primary emitter was a ^{35}Cl nucleus, with a broad excitation energy distribution as inferred from the experiment [6]. The charge distribution was adjusted to reproduce the detected PLF yield in the telescopes and the average detected multiplicities of emitted $Z=1$, 2, and 3 particles. These multiplicities for $Z=1$, 2, and 3 particles with a coincident fragment of $Z_{\max}=10$ were about 4.1, 1.2, and 0.7, respectively. The mean excitation energy was 100 MeV at 30 MeV/nucleon and 150 MeV at 43 MeV/nucleon. (2) The recoil velocity of the primary QP was taken from the inclusive $Z_{\max}$ spectra in the telescopes. Its angular distribution is peaking at the grazing angle and decreases exponentially from the grazing angle with parameters adjusted to yield approximately the angular distribution of the detected PLF. (3) The decay of the primary excited QP was described by the statistical decay code GEMINI [43] which will be described in Sec. IV. (4) Its mean angular momentum around $10\hbar$ was chosen for both incident energies, as estimated by the DIT model. In fact, in the frame of the primary fragments, the LCP's are not emitted isotropically, although the emission pattern is symmetric around 90°. For each decay, the laboratory velocities, energies and emission angles of the PLF and of the associated LCP's as well as their atomic number and mass were registered. The simulated data were then analyzed in the same way as the experimental ones. The left panel of Fig. 6 shows the detected PLF yield distribution in the telescopes and the right panel the corresponding velocity distributions of fragments with $Z_{\max}=10$. The experimental data are satisfactorily reproduced by the simulation with reasonable values for the parameters.

Figure 7 shows typical experimental angular distributions $d\sigma/d\Theta_{\text{c.m.}}$ of $Z=1$, 2, and 3 particles coincident with $Z_{\max}=10$ fragments detected by the telescopes at 30 and 43 MeV/

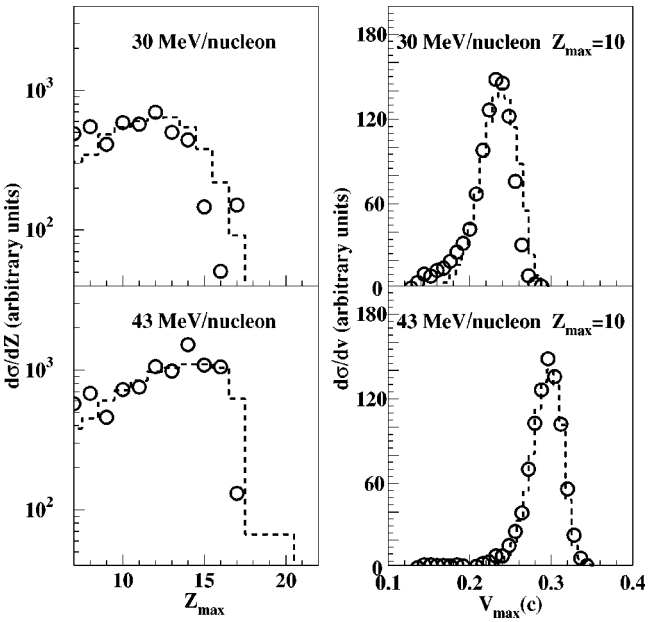

FIG. 6. The charge (left) and velocity distributions (right) of the event largest fragment ($Z_{max}=10$) detected by telescopes at 30 and 43 MeV/nucleon. The circles and lines represent the experimental and filtered simulation results, respectively.

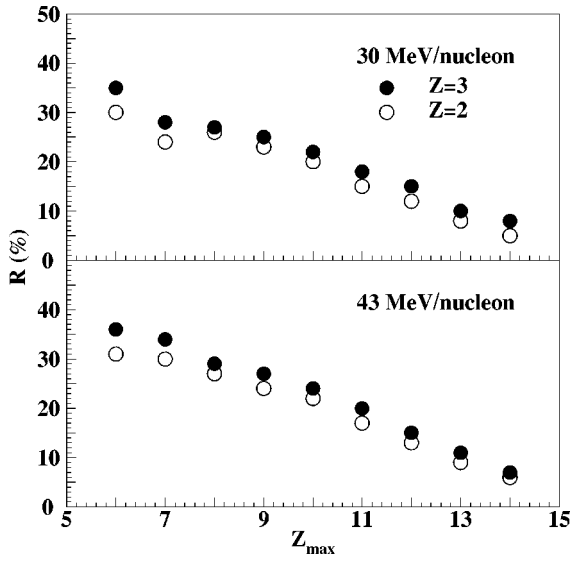

FIG. 8. The fraction of nonequilibrium to equilibrium emitted particles of $Z=2$ and 3 as a function of atomic number of the largest fragment in each event detected by telescopes in ^{35}Cl $+^{197}$Au reaction at 30 and 43 MeV/nucleon.

nucleon. For a given $Z_{\max}$, data from the three telescopes were combined. The angular distribution in the emitter frame was reconstructed from all detected charged particles in each event. The angular distributions for particles coincident with other values for $Z_{\max}$ are similar. As several particles may be emitted, this frame transformation can only be made approximately. Thus recoil effects due to nondetected particles are not taken into account. In the figure, the experimental angular distributions are very asymmetric. As for the velocity distribution, there are more particles emitted in the backward direction. The dotted lines are the angular distributions predicted by a Monte Carlo simulation. In the emitter frame, particles from a statistical emission should display angular distributions symmetrical around 90°. The filtered simulation yields are represented with solid lines. The forward bump is enhanced relative to the backward one because of a Jacobian effect resulting from the strong focusing in the laboratory of the forward emitted fragments. The excellent agreement between the simulated and experimental proton angular distributions suggests an emission from a primary QP in thermal equilibrium. In contrast there is a large excess of backward emitted $Z=2$ and 3 particles when compared to the simulation. This excess is an indication of some ''nonequilibrium emission process.''

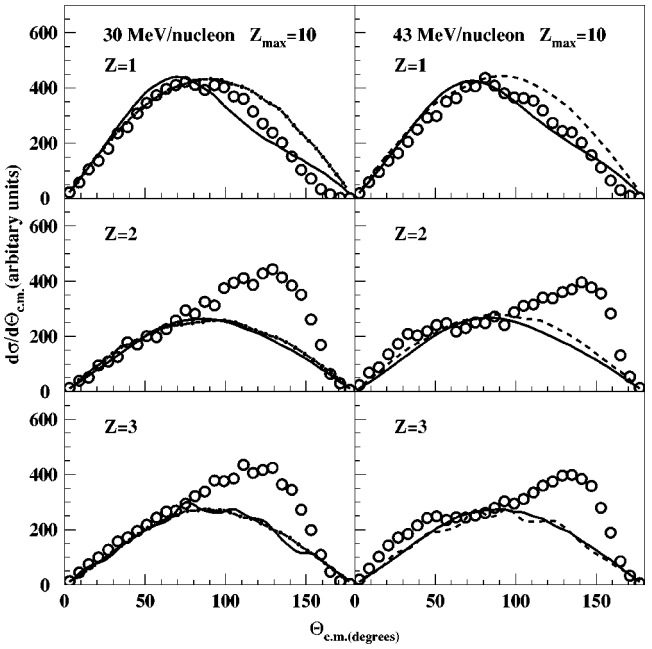

FIG. 7. Experimental angular distributions of $Z=1$, 2, and 3 particles in the emitter frame of events with a heaviest fragment detected by telescopes of charge $Z_{\max}=10$. The dashed and solid lines represent the unfiltered and filtered predictions of Monte Carlo simulations, respectively. For comparison purpose, these curves have been normalized to experimental data at forward angles ($\Theta_{\text{c.m.}}\leqslant 90°$).

With the confidence gained from the simulation for QP decay, the contamination of the QT evaporation could also be estimated from the same Monte Carlo simulation. The primary QT was ^{197}Au, its velocity and deflection angle being calculated from the recoil of a QP event by event. The excitation energy division between QP and QT is supposed to be equipartition (equal sharing). The total excitation energy of QP and QT are deduced from total kinetic energy loss (TKEL). The evaporation particles from QT's were then analyzed in the same way as that from QP's. The simulation shows that the yields for the primary QT can be ignored.

3. The fraction of nonequilibrium emission

With the help of simulations, the fraction of nonequilibrium emission from the QT can be extracted. Figure 8 shows the fraction of particle $Z=2$ and 3 as a function of the heaviest fragment $Z_{\max}$ detected by the telescopes. Nonequilibrium $Z=1$ particles could not be observed unambiguously. For $Z=2$ and 3, one sees from the figure that the fraction

decreases with increasing Z_{max} but, for a given fragment, it is larger for an emitted particle of higher Z. These qualitative results are consistent with those of $^{40}Ar+^{nat}Au$ at 58.7 MeV/nucleon [57]. For a same fragment and a same emitted particle, the fraction in the present system increases slightly with incident energy. It should be pointed out that the above results are qualitative. Quantitative calculations depend critically not only on the geometry of the detectors but also on an accurate energy calibration for the LCP's, as seen in [57]. Variations of the parameters used in the simulation such as recoil velocity, excitation energy, angular distribution, angular momentum of the emitter, do not change the above conclusions. More precise exclusive measurements are desirable for further study.

The presence of a nonequilibrium component is a challenge for calculations of the collision dynamics between complex nuclei [57]. Indeed most preequilibrium calculations do not include composite particle emissions. There are some calculations to explain the origin of nonequilibrium contributions [58–60]. An emission from the zone of overlap between projectile and target would be consistent with the present observation. There are several indications that the observed IMF may have resulted from the rupture of a ''neck'' formed transiently between the reaction partners [15,18,27,28]. During the separation stage, such a neck may be unable to react adiabaticaly to the violent forces exerted on it by fast-moving massive fragments and may snap in two or more points. As a result, a neck residue, a relatively light fragment, would emerge and be accelerated by the mutual Coulomb repulsion.

C. Dissipative collision phenomena

1. Dissipative collision phenomena

Although the dissipative process of heavy-ion collisions at intermediate energies is very close to DIC known at lower energies, there are two differences: the production of QP and QT are accompanied by preequilibrium emission and even the breakup of projectile might occur before the DIC process; most of the dissipated energy is transferred into excitation energy of the partners in the collision. The primary QP and QT are highly excited, so they are short lived (10^{-18}–10^{-16} s). Their observables cannot be measured directly as in lower energies, it has to be inferred from observed products. So the dissipative processes can only be studied from those reconstructed observables. These data could be described using two different hypotheses. (I) An abrasion-ablation mechanism leading to barely excited primary fragments. (II) A binary reaction mechanism reminiscent of DIT where a large amounts of excitation energy is shared between the two partners [57].

In fact, the dissipative binary collision is not as simple as a two step process. The damping process may be accompanied by nonequilibrium particle emission, as described in the previous part. In the present experiment, all products from the QP decay are well above the detection thresholds and their charges are well identified. Particles from the QT are hardly detected. As an approximation, the total detected charge Z_{tot} was used as a global variable to study the dissipative collisions of the present system in a qualitative way. Figure 9 is an illustration of the linear contour plots of

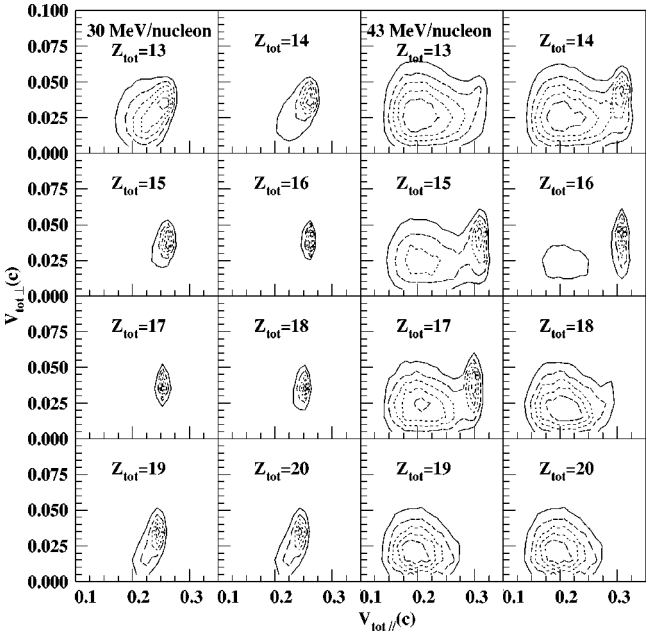

FIG. 9. Linear contour plots of Galilean-invariant cross sections for different total detected charges $Z_{tot}=13$ to 20, in the $^{35}Cl+^{197}Au$ reaction at 30 and 43 MeV/nucleon as a function of $V_{tot\|}$ and $V_{tot\perp}$.

Galilean-invariant cross sections for Z_{tot} from 13 to 20 as a function of $V_{tot\|}$ and $V_{tot\perp}$. For 30 MeV/nucleon, it is very clear that, as Z_{tot} gets close to $Z_{QP}=17$, the velocity distribution becomes narrower. The evolution of the kinetic energy of Z_{tot} is well known in DIC at low energies. So, for 43 MeV/nucleon, such an evolution is not as obvious as for 30 MeV/nucleon. The velocity spectra are strongly peaked as expected in a fragmentation process; however, the fact that the peaks are slightly below the beam velocity and the presence of strong low velocity tails indicate that dissipative phenomena are still acting at 43 MeV/nucleon.

The observation of a characteristic correlation between the amount of dissipated kinetic energy and the deflection angles of the PLF has played an important role in studying the dynamics of damped reactions at lower energies. The observation of such correlations has led to the introduction of a friction force in heavy-ion physics and to the development of various models of dissipative interaction dynamics. Such correlations visualized in a two-dimensional (Wilczyński plot [61]) plot of the yield versus the deflection angle and the kinetic energy of the PLF, have revealed the evolutionary character of the underlying process. Figure 10 shows contour plots of the deflection angle, $\Theta_{c.m.}$, and the associated kinetic energy, E_{tot} for different Z_{tot} from 13 to 20. Since the velocity of a system can be an evaluation of the dissipated energy, this figure may be regarded as an analog of the Wilczyński plot. As seen in this figure, the degree of energy dissipation is strongly correlated with the deflection angle, indicative of a dissipative orbiting process. Clearly, an increasing amount of kinetic energy is converted into heat, as the interacting dinuclear complex turns toward smaller angles. Classical model calculations could account for the main ridge of observed yields and a continuation of this ridge into the range of negative scattering angles, what is also observed in the figure. More dissipative character is ob-

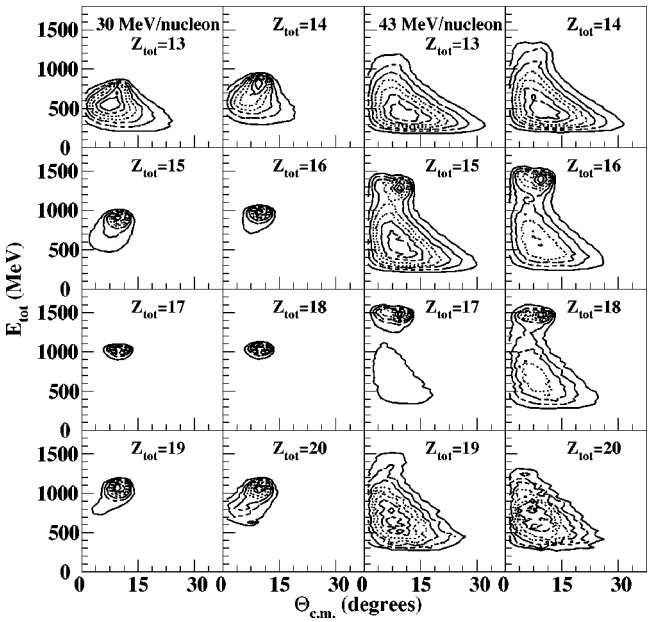

FIG. 10. Linear contour plots of the yield distributions, for different total detected charges Z_{tot}, versus the deflection angle in the c.m., $\Theta_{c.m.}$, and the associated total kinetic energy, in the $^{35}Cl + ^{197}Au$ reaction at 30 and 43 MeV/nucleon.

served at 30 MeV/nucleon than at 43 MeV/nucleon, as it was in the two-dimentional velocity plot.

2. Incomplete dissipative collision phenomena

Dissipative collisions become more complex at intermediate energies. A new mechanism called ''incomplete deep-inelastic scattering'' or ''dissipative fragmentationlike'' reactions [29,33] has been observed experimentally. This could be studied by observing a strong left-right asymmetry of the nonequilibrium particles detected in coincidence with massive fragments. To demonstrate such a mechanism for the present system and further study the dissipative collision in the Fermi energy domain, correlations between weakly damped massive fragments and particle $Z \geqslant 2$ have been measured. Figure 11 shows the angular distributions of particles $Z \geqslant 2$ coincident with fragments $Z_{max}=6$, 7, 8, and 9 for 30 and 43 MeV/nucleon. The fragments with $V_{max} \geqslant 70\% v_{beam}$ were detected by three telescopes. The data from the telescopes were combined. The relative azimuthal angle of coincident particles was limited to $|\Delta\varphi| = |\varphi_1 - \varphi_2| \leqslant 10°$. The solid angle of the different detectors has been taken into account. The angular correlations peak at negative angles, meaning that more coincident particles are emitted in the opposite side of the detected fragments. This is seen as a qualitative manifestation of the direct breakup mode in the dynamical sense [62], because such an asymmetry could not be explained if all coincident particles are emitted from an equilibrated QP. A classical model provides the following picture of the breakup process: in a semiperipheral collision, a projectile coming close to the target is strongly decelerated by the friction force, which breaks the link between clusters in the projectile. For all ejectiles there is a clear correlation between their energy loss and the angle of emission. The target-distant part of the projectile is only slightly deflected and decelerated, while the target-close part

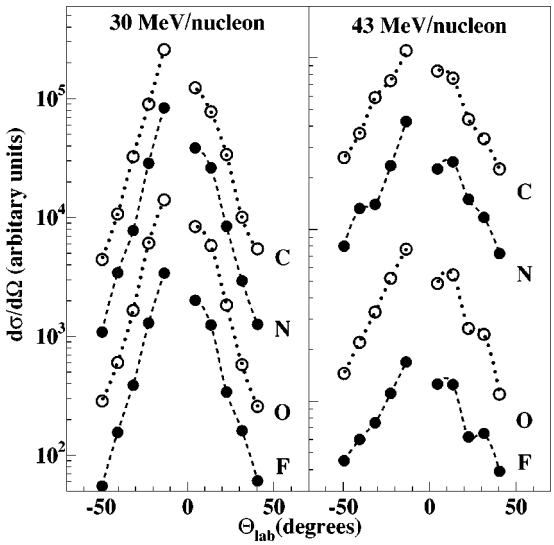

FIG. 11. Angular distributions of particles $Z \geqslant 2$ (mostly alphas and lithiums) coincident with fragments, $Z_{max}=6$, 7, 8, and 9, detected by three telescopes at an angle of 4.0°.

is slowed down orbiting around the target to actually negative scattering angles whereas the particles are preferentially emitted in forward directions with only a slight change in momentum. The whole reaction proceeds on a short time scale, without passing through a phase of thermal equilibration as a necessary intermediate step for the particle emission. The asymmetry of angular distributions shows a dependence on the fragment charge; less asymmetry is observed for a larger Z_{max}. The more violent the collision is, the larger is the yield of incomplete DIC. The fragment angular distributions are more asymmetric at 30 MeV/nucleon than at 43 MeV/nucleon, but smaller cross section for such a mechanism at higher energy could be seen from the data analyses.

IV. MODEL CALCULATIONS AND COMPARISON TO DATA

A. Theoretical models

1. BUU model

The BUU equation [38,63] has been used to understand the collision dynamics. It describes the time evolution of the single-particle phase-space distribution function and observables are calculated from that function. The detailed description of BUU equation can be found in Refs. [38,63]. In the calculations, the equation was solved numerically using a parallel ensemble method. Two different parameter sets were used for the equation of state (EOS), corresponding to values of nuclear compressibility of $K=200$ MeV (soft EOS) and $K=380$ MeV (stiff EOS), respectively. For simplicity, the in-medium nucleon-nucleon cross section $\sigma_{nn} = \int (d\sigma_{nn}/d\Omega) d\Omega$ is chosen to be isotropic and energy independent. The mean field and the Pauli-blocking factors in the collision integral are averaged over an ensemble of 200 parallel simulations. Only test particles with local density exceeding 7% of saturation nuclear density are considered to be part of a bound cluster.

2. Deep inelastic transfers model (DIT)

The DIT model [37] has been used to interpret the formation of an excited QP by dissipative processes. The model is based on the Randrup's one-body dissipative theory [64] which assumes that the dissipation proceeds mainly through stochastic transfers of nucleons decoupled in time. In the model, the system is represented as two Fermi-Dirac gases. The projectile and target approach each other along Coulomb trajectories until they are within the interaction radius. At this point a window defined by potential barriers opens and stochastic transfers, which exchange nucleons, energy, and angular momentum, may occur. The transfer probability is calculated via a phase-space integral which, accounting for the Pauli blocking, incorporates the phase-space flux term, the barrier penetrability, and the occupation probabilities. The transfers generate the fluctuations of mass, charge, excitation energy, and angular momentum. After the interaction, the primary QP and QT follow separate Coulomb trajectories and decay by evaporation into secondary residues.

3. Statistical decay models

The excited QP decay is described with two different statistical decay models. One is a standard sequential binary model GEMINI [43], another one is a simultaneous breakup model SMM [48,65], the latter strongly dependent on the ''freeze-out'' volume. In the GEMINI code, all the possible binary channels from light particle emission to symmetrical division are considered. For the light particle ($Z \leqslant 2$) evaporation the decay width is calculated by using the Hauser-Feshbach formalism [66]. For the emission of heavier fragments ($Z \geqslant 3$) the decay width is determined by using the transition state formalism of Moretto [67]. In the SMM model, the multifragmentation of highly excited nuclei is based on the statistical approach of microcanonical approximations and a liquid drop description of hot primary fragments ($A_F \geqslant 5$). It is assumed that an excited nucleus expands to a certain volume and then breaks up into nucleons and hot fragments. After breakup of the system, the fragments propagate independently in their mutual Coulomb fields and undergo secondary decays. The deexcitation of large fragments ($A_F \geqslant 17$) is described by the evaporation-fission model and for smaller fragments by the Fermi breakup model. The evolution of nuclear disintegration mechanisms with increasing excitation energy, from compound nuclear to multifragmentation and vaporization, follows naturally from the model [68].

4. Hybrid approach

The BUU model used in the present study is more rigorous than the DIT model to describe the collision dynamics as it takes into account two-body collisions and pre-equilibrium emissions, which are not explicitly treated in the DIT model. Nevertheless the DIT model remains interesting. First, one of our main objectives is to study the dissipative processes in the Fermi energy domain. The major features of such processes for $^{40}Ar + ^{nat}Ag$ system at 27 and 44 MeV/nucleon have been reproduced satisfactorily by the model [37]. Secondly, the BUU model does not include the fluctuations, the net mass transfer being always in one direction for a given impact parameter: more nucleons are transferred from the lighter projectile to the heavier target than vice versa. This behavior is well known for an asymmetric heavy-ion reaction at low energies. So the formation of heavy QP's could not be well predicted with the BUU model. However we have calculated the mean number of nucleons transferred from projectile to target and vice versa as a function of impact parameters with the DIT model for $^{35}Cl + ^{197}Au$ at 30 MeV/nucleon. It predicted that the mean number of nucleons transferred between projectile and target have a near linear dependence on the impact parameter and there are more nucleons transferred from the projectile to the target than the net number of transferred nucleons. The results are consistent with that of the BUU model. A similar conclusion has also been obtained by the BUU calculations for the $^{40}Ar + ^{159}Tb$ system at 44 MeV/nucleon [69]. Moreover, the DIT model considers the fluctuations of transfers and allows computation of observables such as mass, excitation energy and angular momentum of QP on an event by event basis. These observables, together with deflection angle and velocity of QP are used as input to the statistical decay model which describes the subsequent decay of the excited QP. A hybrid approach which couples DIT and statistical decay models (GEMINI and SMM) has been established to explain the experimental data.

For a systematic study with sufficient statistics, we generated a total of more than 100 000 events in the simulations. The number of events generated at a given impact parameter is proportional to its value. So the number of events contained in a given domain of observables is proportional to the cross section. The maximum impact parameter estimated from the total reaction cross section given by the semiempirical parametrization [70] is 12.6 fm, corresponding to the 4.3 b geometric total reaction cross section.

Before the simulation results can be compared with the experimental data, the simulated events have to undergo the experimental filter. The filter takes into account the following effects. First, the direction and energy of the emission particles should meet the needs of geometrical and energy cuts of the detection apparatus described in Sec. II. Secondly, two or more particles could not be detected in the same detector during the experiment (multiple hit events). Thirdly, the simulation events are selected in the same way as experimental ones, as it will be described later. In the following comparison of hybrid approach calculations with experimental data, these effects have been considered.

B. The reconstruction of quasiprojectile

1. Event selection

To ensure that the detected particles are emitted from a QP, careful event selection is considered. In the present experiment, at least three kinds of contamination could be present. Contaminations due to the target evaporation and particles emitted from an intermediate-velocity source or nonequilibrium processes as discussed in the previous section. Particles emitted from the preequilibrium processes may also be detected. Since their velocities can extend to several times that of the projectile. Most of preequilibrium particles are concentrated at a small angle along the beam direction.

The event selection followed the method of Désesquelles [71] which is an effective way to eliminate the above contamination [72]. The procedure employed involves three steps: a first evaluation was made by calculating the c.m. of all the particles with charge $Z \geqslant 4$. A more accurate evaluation was then made by retaining only the particles with charge $Z \geqslant 3$ which were included in a velocity selection sphere centered on the first calculated c.m. in velocity space. The radius of the sphere was set to $v = 0.44 v_{\mathrm{beam}}$, so to include all particles emitted in the forward direction. In the third step, this process was repeated including $Z = 2$ and $Z = 1$ particles for which the appropriate velocity radii were set to $0.44 v_{\mathrm{beam}}$ and $0.55 v_{\mathrm{beam}}$, respectively. The radii of the velocity sphere were chosen by Monte Carlo simulations with a statistical evaporation code to ensure that the evaporation particles from highly excited QP's were included and preequilibrium particles were eliminated in a reasonable way. The radii of the velocity sphere have been varied within 10% without influence on the results discussed later. At the selection procedure, about 90% of total events are preserved and less than 5% of $Z = 2$ and 3 particles may account for the contamination of nonequilibrium emission.

To study the decay of excited QP and compare with the model predictions more quantitatively, we concentrate on the events of charged particle multiplicity $M_c \geqslant 2$ and total detected charge $Z_{\mathrm{tot}} = 17$, which correspond to the primary QP's of chlorine isotopes, $Z_{\mathrm{QP}} = 17$, if all particles are from the QP. For lighter Z_{QP}, the contamination due to heavier QP's by missing one or two particles has to be considered. For heavier Z_{QP}, the QP yields are suppressed strongly. To get an overview of the collision, the differential cross section for $Z_{\mathrm{QP}} = 17$ has been simulated with DIT+GEMINI hybrid approach for 30 MeV/nucleon. The results show that the CRL-Laval Array has a strong selection in impact parameter. At small impact parameter ($b \leqslant 4.0$ fm), the deflection angle of QP is larger than 46.8°, and then the QP decay products would rarely be completely detected. We are also not able to detect the events for a large impact parameter ($b \geqslant 12.0$ fm), since it is limited by charged particle multiplicity ($M_c \geqslant 2$) because of the low QP excitation. The multidetector array has a large efficiency for an impact parameter between 6.0 fm and 10.0 fm, and is suitable to study the reaction mechanisms in peripheral and semiperipheral collisions for the present reaction system. After experimental filtering, about 20% of total simulation events were preserved. For totally detected charge $Z_{\mathrm{tot}} = 17$ events, the hybrid approach predicted that 90% events originate from the decay of $Z_{\mathrm{QP}} = 17$, and 7% and 3% events from the decay of $Z_{\mathrm{QP}} = 18$ and 19, respectively. The values are very close to the experimental result of 92% (17), 6% (18) and 2% (19), which were estimated by considering the measured cross section and detection efficiency [72].

2. The reconstruction of quasiprojectile

Assuming that all the QP products are detected, then the velocity and excitation energy of primary QP's can be reconstructed from their decay products on an event by event basis by energy and momentum conservation laws. The velocity of a QP, V_{qp}, is the vector sum of the product velocities. Its excitation energy E^*_{qp} was obtained by combining the Q value of the detected channel to the relative kinetic energy:

$$\mathrm{E}^*_{\mathrm{qp}} = \frac{1}{2}\sum_n m_n |\vec{v}_n - \vec{V}_{\mathrm{qp}}|^2 - Q_{\max} + E_n . \qquad (1)$$

The sum runs over the number of products and v_n and m_n are the product velocity and mass. Q_{max} is the most positive Q value of each detected channel. A correction for unobserved neutrons E_n was made using an empirical law for neutron multiplicity and a kinetic energy per neutron equal to $2T$. The temperature T was estimated from a first step excitation energy which does not include the E_n.

C. The production of quasiprojectile

1. Dynamical simulations of BUU model

The BUU model has been used to simulate the dynamical evolution of collisions with impact parameters and incident energies. Figure 12 displays the mean density profiles in the reaction plane for BUU simulations with stiff EOS as a function of time, for three impact parameters at (a) 30 MeV/nucleon and (b) 43 MeV/nucleon incident energies. The calculations were followed up to 400 fm/c relative to the instant when the projectile and target surfaces are separated by 2.0 fm at $t = 0$ fm/c. Two features should be noted in the figure. First, for peripheral collisions of large impact parameter, $b = 10.0$ fm, after about a time of 120 and 100 fm/c, well defined primary QP and QT can be identified at 30 and 43 MeV/nucleon, respectively. For semiperipheral collision of $b = 7.0$ fm, it takes more time, about 220 and 160 fm/c. So the lifetime of a dinuclear system depends not only on the impact parameter but also strongly on incident energies. It decreases with incident energy and impact parameter. Obviously a single deformed compound nucleus is still formed until $t = 400$ fm/c in the calculation at small impact parameter (4.0 fm) for both incident energies. Secondly, the characteristics of the primary QP calculated with a dynamical model are also sensitive to the freeze-out time at which those observables are evaluated.

To understand the effect of nucleon-nucleon collision terms, BUU model without a collision term was also simulated for both incident energies. As expected, the effect of the collision term increases with incident energy. At 30 MeV/nucleon, an essential feature of the calculations is the exchange mediated by mean field, between projectile and target of nucleons that do not undergo a collision. This nucleon exchange is very similar to that associated with the so-called window-wall approximation of one-body dissipation used for low energy reactions. Figure 13 shows the BUU predictions with soft EOS for the mass, deflection angle, velocity, angular momentum of the primary QP for the two incident energies. The QP is referred as the second largest fragment at the end of the calculation. A simple geometrical cut was used to assign a test particle to either the primary QP or QT. The angular momentum was calculated in a classical approximation. The mean freeze-out times were chosen as 160 fm/c and 130 fm/c for 30 and 43 MeV/nucleon respectively, but slight differences were made for different impact parameters. In the figure, the mass of primary QP decreases with impact parameter for both energies. At large impact

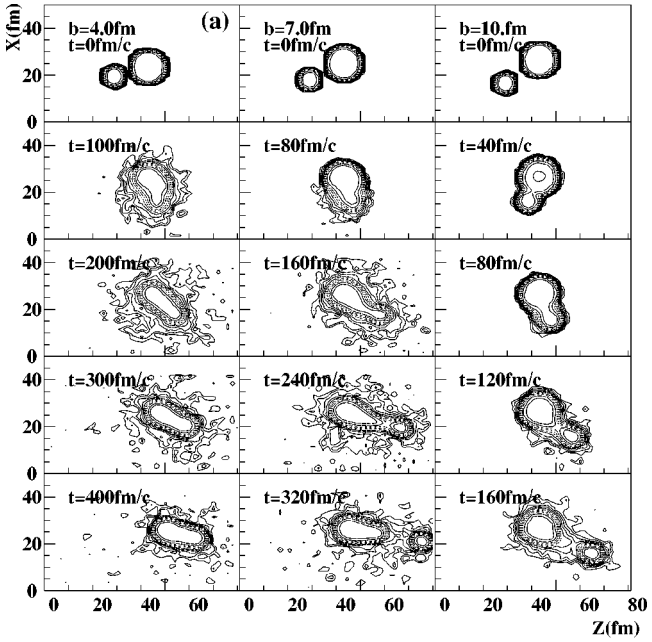

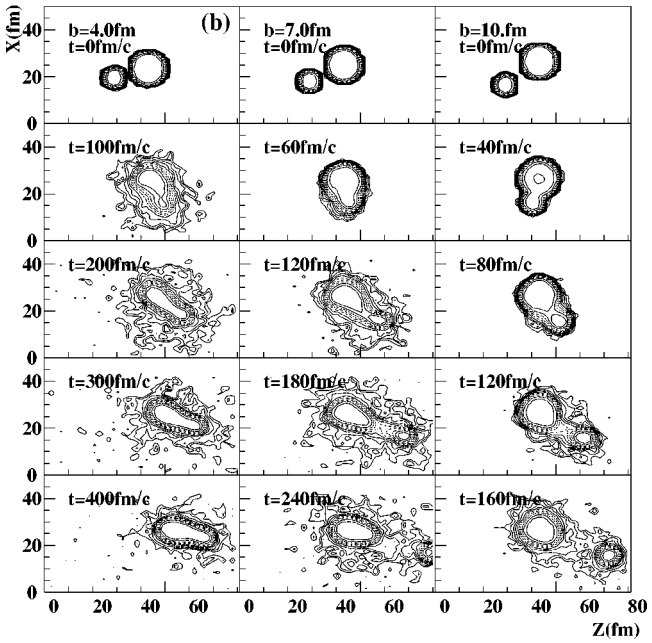

FIG. 12. The mean density profiles of BUU simulation in the reaction plane with time evolution of the $^{35}\mathrm{Cl}+^{197}\mathrm{Au}$ reaction at different impact parameters for (a) 30 MeV/nucleon and (b) 43 MeV/nucleon incident energies. The density value is on a logarithmic scale.

parameter, the mass of QP was about 29, most of lost nucleons were emitted as preequilibrium particles. At small impact parameter, the mass of the primary QP is predicted smaller at 43 MeV/nucleon than at 30 MeV/nucleon. More interesting is the evolution of deflection angle with impact parameter and the incident energy. As shown in the figure, the mean scattering angle of QP is about 0° and less dependent of impact parameter at 43 MeV/nucleon. However, at 30 MeV/nucleon, the deflection angle of QP is negative for most impact parameters and as large as $-15°$ for an impact parameter of 6 fm. The velocity of primary QP was normalized to that of the projectile. It decreases smoothly with im-

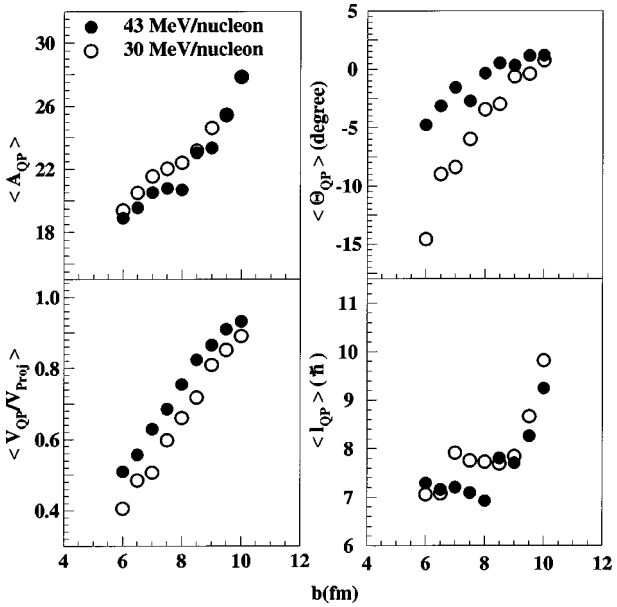

FIG. 13. The distributions of four observables for the primary QP as a function of impact parameter from BUU calculations for the $^{35}\mathrm{Cl}+^{197}\mathrm{Au}$ reaction at 30 (open circles) and 43 (full circles) MeV/nucleon. $\langle A_{\mathrm{QP}}\rangle$,$\langle \Theta_{\mathrm{QP}}\rangle$,$\langle V_{\mathrm{QP}}\rangle$, and $\langle l_{\mathrm{QP}}\rangle$ are the average mass, laboratory frame deflection angle, velocity and angular momentum of the primary QP, respectively. In the figure, the average velocity was normalized by that of projectile, V_{proj}.

pact parameter. At the same impact parameter, the QP was observed to be slower at 30 MeV/nucleon than at 43 MeV/nucleon. The smaller deceleration of the QP may be explained from a shorter interaction time. One notices that for a given impact parameter ($b \geqslant 8$ fm) the angular momentum is almost the same at both incident energies, but there is a plateau at small impact parameter ($b \leqslant 8$ fm). The angular momentum is higher at 30 MeV/nucleon than at 43 MeV/nucleon at impact parameter $b \approx 7.5$ fm. The small difference for the angular momentum is very similar to that for the mass. A possible explanation of the similar behaviors could be the more dominant nucleon-nucleon collision at smaller impact parameter and higher incident energy from a comparison with BUU simulations neglecting collision terms.

Figure 14 shows the correlation between the recoil velocity and deflection angle of primary QP with two kinds of EOS at 30 and 43 MeV/nucleon. For 30 MeV/nucleon, the BUU model predicts a decrease in velocity and deflection angle with impact parameter. The collision characteristics are typical of a binary dissipative process observed at low energy. However, such a direct correlation is not so obvious at 43 MeV/nucleon. It should be emphasized that the simulated results of BUU model are qualitative and will be affected by the freeze-out time, EOS and number of test particles, etc.

2. Reconstructed excitation energy of the quasiprojectile

Properties for the primary QP of $Z_{\mathrm{QP}}=17$ have been also predicted by DIT model calculations. Figure 15 shows the mean angular momentum $\langle l_{\mathrm{QP}}\rangle$ and mass $\langle A_{\mathrm{QP}}\rangle$ distributions as a function of excitation energy E^*_{QP} from DIT model calculations at 30 and 43 MeV/nucleon. The $\langle l_{\mathrm{QP}}\rangle$ has a very similar distribution for the two incident energies. The maxi-

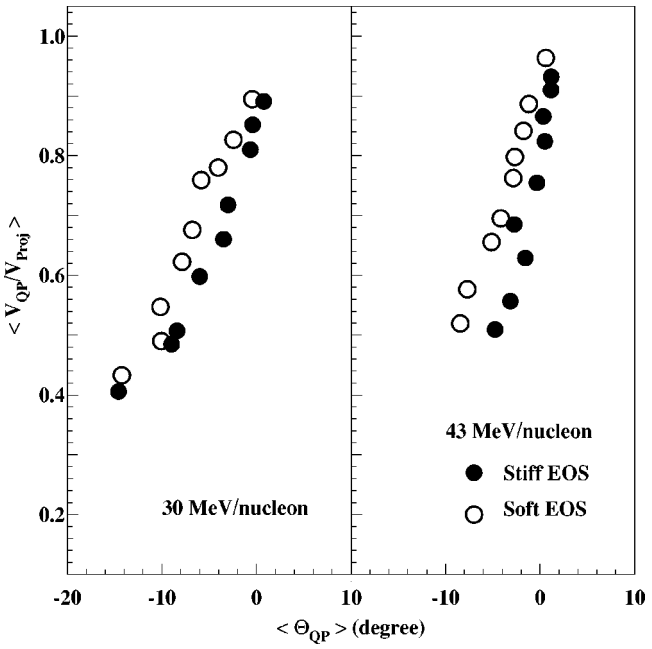

FIG. 14. The correlation between the deflection angle in the laboratory system and the velocity of primary QP from the BUU model for stiff and soft EOS for ^{35}Cl+^{197}Au reaction at 30 and 43 MeV/nucleon. The full and open circles represent the stiff and soft EOS results, respectively.

mum $\langle l_{\rm QP}\rangle$ value $20\hbar$ is reached at the highest excitation energy. The corresponding angular momentum of QT is about $55\hbar$. The value is close to the experimental result for a similar system Ar+Au at 30 MeV/nucleon [59]. On the other hand, the total angular momentum of QP and QT can be estimated in the simple classical model which was used in DIC at low energies. If we suppose the so-called ''sticking limit,'' two spheres of projectile and target sticking together and rotating rigidly prior to break up, the amount of angular momentum transferred to the internal degrees of freedom, Δl, depends on the moments of inertia according to the relationship

$$\Delta l = l_i - l_j = l_i \frac{J_P + J_T}{J_i + J_P + J_T}, \tag{2}$$

where l_i and l_j are the initial and final angular momenta of the system, respectively. J_P, J_T, and J_i are the inertia moments of the projectile, target and system. If l_i is supposed to be $190\hbar$, which corresponds to an impact parameter of about 5 fm, then the Δl, is about $90\hbar$, which is larger than $75\hbar$ predicted by the DIT model. It means that the QT and QP are not fully sticking at the highest energy damping in the DIC collisions.

Another interesting prediction of DIT model is that the QP is neutron-rich. The mean masses of $Z_{\rm QP}=17$ increase with its excitation energy as shown in the lower part of Fig. 15. At the highest excitation energy, the $\langle N\rangle/Z$ ratio is about 1.35 and 1.18 for 30 and 43 MeV/nucleon, respectively, which is larger than that of the projectile ($\langle N\rangle/Z=1.06$) and approaches the value of the compound system ($\langle N\rangle/Z=1.42$). The dissipation of energy and $\langle N\rangle/Z$ increase with the lifetime of the dinuclear complex formed in damped collisions. At the same excitation energy, the lower $\langle N\rangle/Z$ values for the primary QP with higher bombarding energy could be explained by the shorter interaction time at 43 MeV/nucleon. At higher energies, the $\langle N\rangle/Z$ remains that of the projectile as predicted by the fragmentation model [19]. The qualitative behavior of mass evolution with excitation energy of primary QP and incident energy has been indirectly supported by the experimental charged particle multiplicity discussed in the next section.

To check the reconstruction procedure for the kinetic energy and excitation energy of the primary QP from its decay products, simulation events of hybrid approach were analyzed in the same way as the experimental ones. The reconstructed kinetic energy and excitation energy were compared with the values given by DIT model. The reconstructed mean kinetic energy of total detected charge $Z_{\rm tot}=17$ is consistent with the prediction of DIT model for $Z_{\rm QP}=17$. However, the discrepancy increases with decreasing $Z_{\rm tot}$ value because of the recoil effects of undetected particles. After correction for the energy taken by unobserved neutrons, the mean excitation energy is also in good agreement with that of $Z_{\rm QP}=17$. So the energy conservation is precise enough in the simulations and reconstruction process. The main uncertainty of reconstructed excitation energy is due to the mean neutron multiplicity $\langle M_n\rangle$. The $\langle M_n\rangle$, which increases with $E^*_{\rm QP}$ and decreases with increasing incident energies, was estimated by averaging the predictions of hybrid approach and mass balance, where the masses of QP and products were taken from DIT model and previous experiment [6]. At highest excitation energy, the unobserved neutrons are estimated approximately to take as much as 25 and 20% of $E^*_{\rm QP}$ for 30 and 43 MeV/nucleon, respectively.

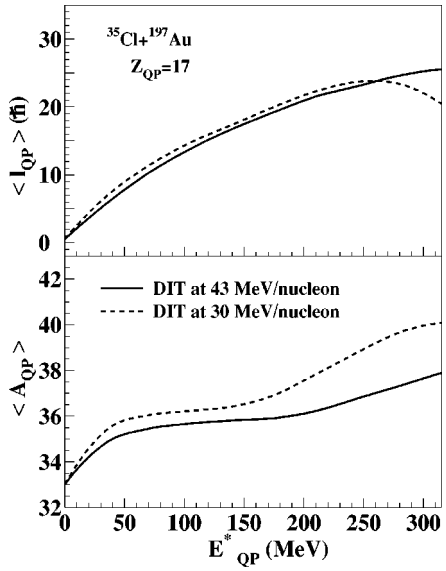

FIG. 15. Mean angular momentum and mass distributions of chlorine as a function of excitation energy from DIT model predictions. The solid and dashed lines represent the results for 43 and 30 MeV/nucleon, respectively.

The excitation energy distributions reconstructed from experimental data for all $Z_{\rm tot}=17$ channels and a comparison with the filtered results of DIT model are shown in Fig. 16 for 30 and 43 MeV/nucleon. The mean $E^*_{\rm QP}$ are around 100 and 120 MeV and energies up to 350 and 400 MeV are

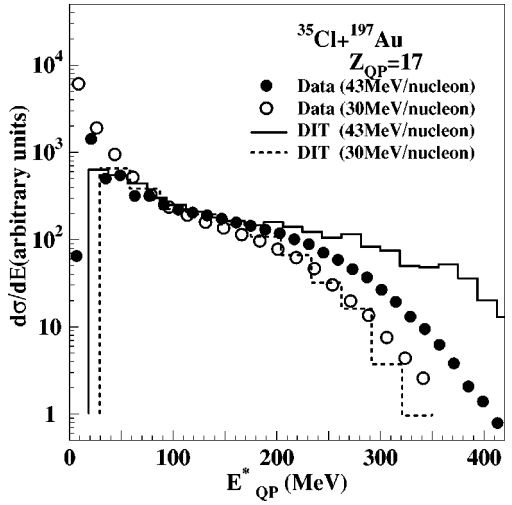

FIG. 16. Excitation energy spectra of chlorine QP reconstructed from the experimental decay products. The full (open) circles and solid (dashed) lines represent the experimental data and the DIT model predictions of ^{35}Cl+^{197}Au system at 43 (30) MeV/nucleon, respectively.

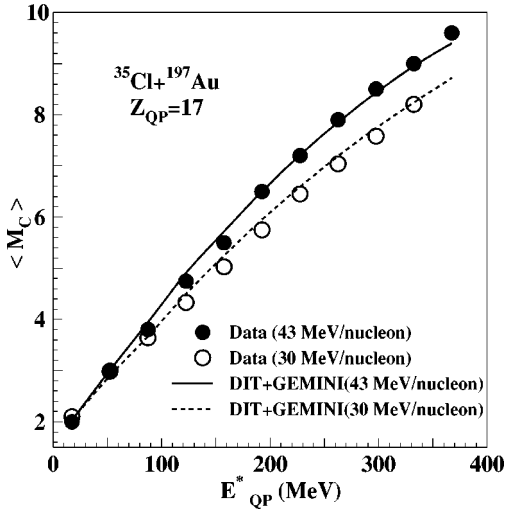

FIG. 17. The mean charged particle multiplicities as a function of chlorine QP excitation energy compared with the predictions of DIT+GEMINI hybrid approach. The solid (open) circles and full (dashed) lines represent the experimental data and the simulation predictions of ^{35}Cl+^{197}Au system at 43 (30) MeV/nucleon, respectively.

obtained for 30 and 43 MeV/nucleon, respectively. The maximum uncertainties of the reconstructed excitation energy is about 10%. The yield of primary QP decreases rapidly with increasing excitation energy. For 30 MeV/nucleon, the DIT model provides a generally good agreement with the experimental data over the entire range of excitation energy. But for 43 MeV/nucleon, DIT model overpredicts the yield of highly excited QP. The yield distribution of primary QP is sensitive to its deflection function. The Coulomb trajectories of QP should be modified by considering the proximity potential in DIT model for high incident energies.

D. The decay of excited quasiprojectile

1. Distributions of experimental observables

The simplest variable which can be directly extracted from the experimental data is the charged particle multiplicity M_c, including light charged particle ($Z=1,2$) as well as heavier fragments. This global observable is an indicator of the collision violence and has even been used to distinguish central from peripheral collisions [73]. The multiplicity dependence on the impact parameter is strong in peripheral and semiperipheral collisions, where a near linear dependence is observed [55]. Figure 17 shows the experimental $\langle M_c \rangle$ versus $E^*_{\rm QP}$ of $Z_{\rm QP}=17$ for 30 and 43 MeV/nucleon and a comparison with the predictions of a hybrid approach. In the figure, a strong dependence of M_c on $E^*_{\rm QP}$ is observed for both incident energies. Multiplicities as high as 8 and 9 are reached at the highest excitation energy for 30 and 43 MeV/nucleon, respectively. The difference of $\langle M_c \rangle$, by about one unit for the two energies at the highest excitation energies, might result from mass differences of chlorine QP's as shown in Fig. 16, and can be explained by the hybrid approach. The hybrid approach predicts that the impact parameters $b=7$, 8, 9, 10, and 12 fm of 30 MeV/nucleon correspond to $\langle M_c \rangle = 5.76$, 4.64, 3.03, 2.35, and 2.15, respectively.

To characterize the decay of excited QP's, several observables are used: the average multiplicity of IMF($3 \leqslant Z \leqslant 8$), $M_{\rm IMF}$, the average maximum charge of fragments, $Z_{\rm max}$, the average asymmetry of the two largest fragments, A_{12}, and the average asymmetry of second and third largest fragments, A_{23}, $A_{12}=(Z_{\rm max}-Z_2)/(Z_{\rm max}+Z_2)$, and $A_{23}=(Z_2-Z_3)/(Z_2+Z_3)$, where Z_2 and Z_3 are the second and third largest fragment charges. $M_{\rm IMF}$ characterizes the degree of disintegration of the excited nucleus and $Z_{\rm max}$, A_{12}, and A_{23} reflect the sizes of the fragments. The whole set of these observables gives a rather complete description of the fragmentation pattern [65]. Figure 18 shows the dependence of those observables on the excitation energy of $Z_{\rm QP}=17$. The $\langle M_{\rm IMF} \rangle$ increases monotonically with increasing energy, reaches a saturation value of $\langle M_{\rm IMF} \rangle \approx 1.4$ at $E^*_{\rm QP} \approx 300$ MeV and then appears to decrease. The experimental distribution of $\langle Z_{\rm max} \rangle$ decreases simply with the increase of $E^*_{\rm QP}$. The $\langle A_{12} \rangle$ exhibits a similar dependence as $\langle Z_{\rm max} \rangle$ with the excitation energy, whereas the $\langle A_{23} \rangle$ is almost independent of the excitation energy at high excitation energies ($E \geqslant 100$ MeV). At lower excitation energies ($E \leqslant 100$ MeV), $\langle A_{23} \rangle$ has a large fluctuation because of the smaller charged particle multiplicity. The mean observable distributions as a function of excitation energy show very similar tendency for both incident energies. The independence of the incident energies gives us a strong experimental evidence that the QP might approach thermal equilibrium and has similar primary characteristics at 30 and 43 MeV/nucleon incident energies [74,75].

The experimental distributions presented in Fig. 18 were compared with the calculations of GEMINI and SMM models. In the simulations, the recoil velocities and deflection angles of primary QP as a function of excitation energy are extracted from the experimental data to avoid the uncertainties caused by DIT model. However, in the absence of systematic knowledge, the angular momentum and mass values were still taken from the prediction of DIT model. The

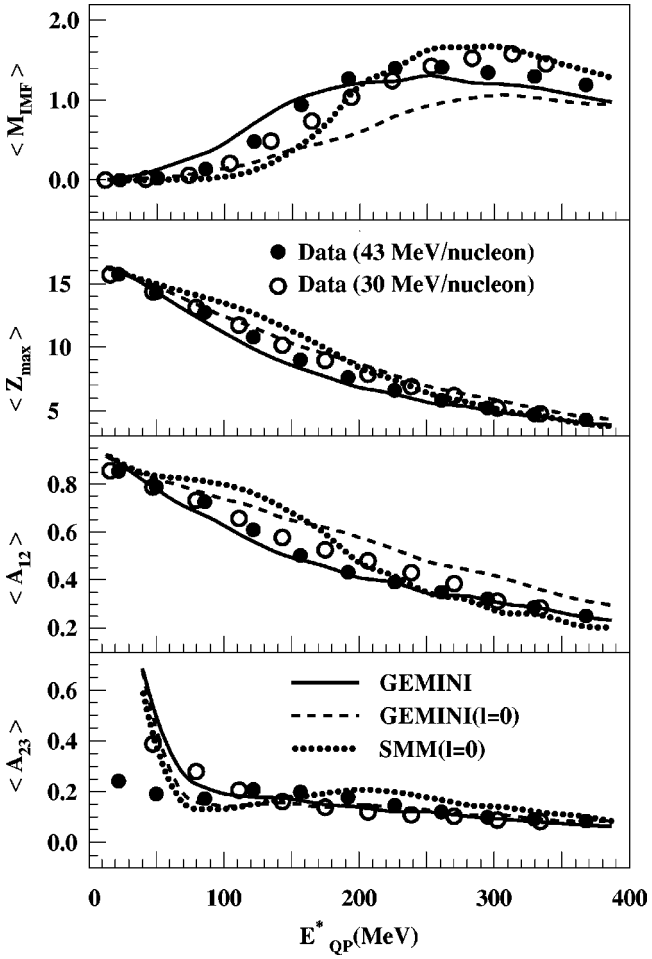

FIG. 18. The mean IMF multiplicity, maximum fragment charge and first and second asymmetry of fragment charge distributions as a function of excitation energy for the ^{35}Cl+^{197}Au system at 30 and 43 MeV/nucleon. The full (open) circles represent the efficiency corrected experimental data of 43 (30) MeV/nucleon. The solid, dashed and dot lines represent the predictions of statistical decay models GEMINI (including angular momentum), GEMINI ($l=0$) and SMM ($l=0$), respectively.

events generated by the statistical model were passed through the experimental filter. The GEMINI simulations have been performed in two steps: without ($l=0$) and with angular momentum respectively. However, in the SMM simulations, the angular momentum has not been considered because of the shortcoming of the code itself. The freeze-out volume is $V=V_0(1+\kappa)$, where κ is a model parameter and V_0 the volume of the system corresponding to normal nuclear matter density, respectively. A value of $\kappa=1$ was used in the SMM simulation. As shown in Fig. 18, the GEMINI simulation which does not include angular momentum, disagrees with the overall distributions of experimental data. After including angular momentum, the distributions have changed considerably and agree with the experimental data satisfyingly. So the angular momentum plays an important role in the decay of hot nuclei [76]. Although the effect of angular momentum has not be considered in the SMM simulation, the SMM calculation can also reproduce the experimental data over the entire range of excitation energy. At lower excitation energy, the GEMINI model predicts $\langle M_{\mathrm{IMF}}\rangle$ larger than the SMM model and overpredicts the experimental values. At higher excitation energy, the opposite situation is found. In Fig. 19, experimental inclusive charge distributions of chlorine QP's are compared with the GEMINI and SMM calculations for four excitation energy bins. For the low excitation energy bin, the charge distribution shows two peaks reproduced by GEMINI, but the SMM model underpredicts the yield of IMF's. For higher excitation energies ($E^*_{\mathrm{QP}}\geqslant 100$ MeV), the charge distribution peaks at smaller values and it is equaly well reproduced by SMM and GEMINI. A qualitatively similar behavior was also observed in the decay of heavier QP, $Z_{\mathrm{QP}}=18$, 19, and 20.

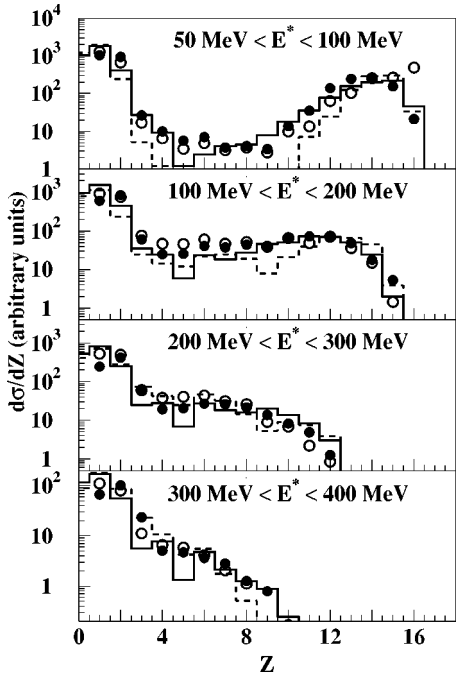

FIG. 19. Experimental inclusive charge distributions for four bins of excitation energy: 50–100 MeV, 100–200 MeV, 200–300 MeV and 300–400 MeV. The full (open) circles represent the experimental data of the ^{35}Cl+^{197}Au system at 43 (30) MeV/nucleon. The solid (dashed) lines represent the predictions of GEMINI and SMM model, respectively.

2. The energy spectrum of products

The excitation energy E_k of QP determines also the kinetic properties of its products. Comparisons of experimental and calculated energy spectra of emitted products may provide some further insights into questions such as source size and expansion [77]. To explore the dependence of mean kinetic energy with excitation energy, the $\langle E_K\rangle$ of products for $Z_{\mathrm{QP}}=17$ versus their charge Z in their rest frame are shown in Fig. 20 for four excitation energy bins. In the figure, the $\langle E_K\rangle$ was divided by $2Z$ for comparison. The distributions of $\langle E_K/2Z\rangle$ are again nearly independent of the incident energies in each excitation energy bin, but increase with excitation energy since they are related to the temperature of the emitter. For a given excitation energy bin, the $\langle E_K/2Z\rangle$ decreases with increasing Z. The calculations of GEMINI model underpredict the experimental data of IMF's for all excitation energy bins and the disagreement increases with excitation energy. At lower excitation energies (200 MeV $\leqslant E^*_{\mathrm{QP}}$), the calculated SMM results are in good agreement

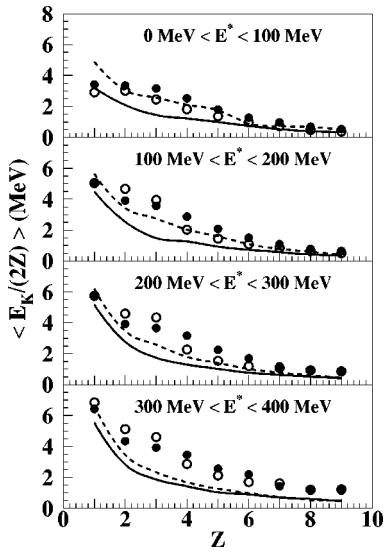

FIG. 20. Experimental mean kinetic energy values of charged products ($1 \leqslant Z \leqslant 9$) evaluated in the reference frame of the primary QP ($Z_{QP}=17$) versus their charges compared with the calculations of GEMINI and SMM models for four bins of excitation energy: 0–100 MeV, 100–200 MeV, 200–300 MeV and 300–400 MeV. The full (open) circles represent the experimental data of the ^{35}Cl $+^{197}$Au system at 43 (30) MeV/nucleon. The solid (dashed) lines represent the predictions of GEMINI and SMM model, respectively.

with the shape of the energy spectra and $\langle E_K/2Z \rangle$ data. With increasing excitation energy, the data for $Z=1$ are still reproduced by the SMM model, but the disagreement with the other data increases. A possible explanation for the additional kinetic energy of IMF's could be the smaller source size or the existence of a collective expansion which gives a larger boost to heavy fragments at higher excitation energy. It could not be accounted for even by the effect of angular momentum. The rotational energy of emitted fragments is weak.

V. SUMMARY AND CONCLUSIONS

In summary, the reactions ^{35}Cl$+^{197}$Au have been studied at 30 and 43 MeV/nucleon in peripheral and semiperipheral collisions. Nonequilibrium α and IMF components have been found to compete with those arising from the statistical evaporation of the QP. The fraction of nonequilibrium emission has been extracted with the help of Monte Carlo simulations. It decreases with larger QP remnant charge, but for a given charge, it increases with the charge of the emitted particles. A proper treatment of nonequilibrium effects with the current microscopic transport model has not yet been worked out. Since the nonequilibrium IMF component can be studied in less violent binary collisions, for which the exit channel is simple and easy to characterize, a very interesting opportunity is offered to study dynamical effects in nuclear reactions under well-controlled experimental conditions.

The QP characteristics have been reconstructed from their decay products with a careful event selection: several features are reminiscent of damped reactions at lower bombarding energies, since the QP atomic number and deflection angle depend strongly on the kinetic energy or dissipated energy. The excited QP is seen to be produced in binary, orbiting-type collisions, compatible with the scenario underlying the nucleon exchange model. The dissipative collision processes have been analyzed in BUU and DIT models. At 30 MeV/nucleon, the experimental data can be explained by DIT model in a consistent way. One-body dissipation is still the main mechanism for the energy and angular momentum dissipation. The number of neutrons and protons transferred between projectile and target has a nearly linear dependence on the impact parameter. However for 43 MeV/nucleon, DIT is able to predict only the experimental tendency. Two-body dissipation might play a more important role at that incident energy.

The similarity of the distributions for the decay products between the two incident energies suggests that the excited QP formed in the binary collision might approach thermal equilibrium. The decay products of the highly excited QP have been analyzed in sequential binary and simultaneous disassembly statistical decay model. Both statistical models are able to provide good agreement with the experimental observables except for the mean kinetic energy of the products. These results concerning final fragment distributions suggest that statistical decay plays a more important role than dynamical fluctuations in the breakup of excited QP's formed in peripheral and semiperipheral events.

ACKNOWLEDGMENTS

This work has been supported in part by the Natural Sciences and Engineering Research Council of Canada and the Fonds pour la Formation des Chercheurs et l'Aide à la Recherche. The authors are very grateful to Dr. R. J. Charity and Dr. L. Tassan-Got for supplying the GEMINI and DIT codes used in this work. X.Q. also acknowledges the kind hospitality extended to him by Laboratoire de Physique Nucléaire, Département de Physique, Université Laval.

[1] D. Guerreau *et al.*, Nucl. Phys. **A574**, 111c (1994).
[2] C. K. Gelbke and D. H. Boal, Prog. Part. Nucl. Phys. **19**, 33 (1987), and references therein.
[3] L. G. Moretto and G. J. Wozniak, Annu. Rev. Nucl. Part. Sci. **43**, 397 (1993), and references therein.
[4] B. Lott *et al.*, Phys. Rev. Lett. **68**, 3141 (1992).
[5] G. Bizard *et al.*, Phys. Lett. B **302**, 162 (1993).
[6] L. Beaulieu *et al.*, Nucl. Phys. **A580**, 81 (1994).
[7] J. Péter *et al.*, Nucl. Phys. **A593**, 95 (1995).
[8] L. Beaulieu *et al.*, Phys. Rev. Lett. **77**, 462 (1996).
[9] H. Fuchs and K. Möhring, Rep. Prog. Phys. **57**, 188 (1994), and references therein.
[10] M. Lefort and C. Ngo, Ann. Phys. (Paris) **3**, 5 (1985).
[11] F. Rami *et al.*, Z. Phys. A **327**, 207 (1987).
[12] M. Morjean *et al.*, Phys. Lett. B **203**, 215 (1988).
[13] B. Borderie *et al.*, Phys. Lett. B **205**, 26 (1988).
[14] M. Morjean *et al.*, Nucl. Phys. **A524**, 179 (1991).
[15] L. Stuttgé *et al.*, Nucl. Phys. **A539**, 511 (1992).

[16] R. J. Charity *et al.*, Z. Phys. A **341**, 53 (1991).
[17] J. F. Lecolley *et al.*, Phys. Lett. B **325**, 317 (1994).
[18] J. Tõke *et al.*, Phys. Rev. Lett. **75**, 2920 (1995).
[19] A. Bonasera *et al.*, Nucl. Phys. **A463**, 653 (1987).
[20] Ch. Egelhaaf *et al.*, Nucl. Phys. **A405**, 397 (1983).
[21] G. Royer *et al.*, Nucl. Phys. **A466**, 139 (1987).
[22] L. G. Moretto and G. J. Wozniak, Prog. Part. Nucl. Phys. **21**, 401 (1988), and references therein.
[23] M. F. Rivet *et al.*, Phys. Lett. B **215**, 55 (1988).
[24] D. Jouan *et al.*, Z. Phys. A **340**, 63 (1991).
[25] J. L. Wile *et al.*, Phys. Lett. B **264**, 26 (1991).
[26] J. L. Wile *et al.*, Phys. Rev. C **45**, 2300 (1992).
[27] C. P. Montoya *et al.*, Phys. Rev. Lett. **73**, 3070 (1994).
[28] J. F. Lecolley *et al.*, Phys. Lett. B **354**, 202 (1995).
[29] W. Terlau *et al.*, Z. Phys. A **330**, 303 (1988).
[30] J. Uckert *et al.*, Phys. Lett. B **206**, 190 (1988).
[31] R. Wada *et al.*, Nucl. Phys. **A539**, 316 (1992).
[32] R. Wada *et al.*, Nucl. Phys. **A548**, 471 (1992).
[33] C. Schwarzt *et al.*, Phys. Lett. B **279**, 223 (1992).
[34] R. Dayras *et al.*, Nucl. Phys. **A460**, 299 (1986).
[35] J. P. Bondorf *et al.*, Nucl. Phys. **A443**, 321 (1987).
[36] J. Randrup, Nucl. Phys. **A327**, 490 (1979).
[37] L. Tassan-Got and C. Stéphan, Nucl. Phys. **A524**, 121 (1991).
[38] W. Bauer *et al.*, Phys. Rev. C **34**, 2127 (1986).
[39] J. Aichelin and H. Stöcker, Phys. Lett. B **176**, 14 (1986).
[40] G. Peilert *et al.*, Rep. Prog. Phys. **57**, 533 (1994).
[41] J. C. Steckmeyer *et al.*, Nucl. Phys. **A500**, 372 (1989).
[42] W. A. Friedman and W. G. Lynch, Phys. Rev. C **28**, 16 (1983).
[43] R. J. Charity *et al.*, Nucl. Phys. **A483**, 371 (1988).
[44] W. A. Friedman, Phys. Rev. C **42**, 667 (1990).
[45] J. Richert and P. Wagner, Nucl. Phys. **A517**, 399 (1990).
[46] J. A. López and J. Randrup, Nucl. Phys. **A503**, 183 (1989).
[47] D. H. E. Gross, Rep. Prog. Phys. **53**, 605 (1990).
[48] A. S. Botvina *et al.*, Nucl. Phys. **A475**, 663 (1987).
[49] C. Pruneau *et al.*, Nucl. Instrum. Methods Phys. Res. A **297**, 404 (1990).
[50] Y. Larochelle *et al.*, Nucl. Instrum. Methods Phys. Res. A **348**, 167 (1994).
[51] D. Fox *et al.*, Nucl. Instrum. Methods Phys. Res. A **374**, 63 (1996).
[52] R. Lucas *et al.*, Nucl. Phys. **A464**, 172 (1987).
[53] O. Granier *et al.*, Nucl. Phys. **A481**, 109 (1988).
[54] C. Vincent-Donnet *et al.*, J. Phys. G **22**, 397 (1996).
[55] A. Del Zoppo *et al.*, Phys. Rev. C **50**, 2930 (1994).
[56] N. Colonna *et al.*, Phys. Rev. Lett. **62**, 1833 (1989).
[57] J. E. Sauvestre *et al.*, Phys. Lett. B **335**, 300 (1994).
[58] L. G. Sobotka *et al.*, Phys. Rev. C **50**, R1272 (1994).
[59] J. Colin *et al.*, Nucl. Phys. **A583**, 449c (1994).
[60] B. Jouault *et al.*, Nucl. Phys. **A597**, 136 (1996).
[61] J. Wilczyński, Phys. Lett. **47B**, 484 (1973).
[62] K. Möhring *et al.*, Nucl. Phys. **A533**, 333 (1991).
[63] G. F. Bertsch and S. Das Gupta, Phys. Rep. **160**, 189 (1988), and references therein.
[64] J. Randrup and R. Vandenbosch, Nucl. Phys. **A474**, 219 (1987).
[65] A. S. Botvina *et al.*, Nucl. Phys. **A507**, 649 (1990).
[66] T. D. Thomas, Annu. Rev. Nucl. Sci. **18**, 343 (1969).
[67] L. G. Moretto, Nucl. Phys. **A247**, 211 (1975).
[68] J. P. Bondorf *et al.*, Phys. Rep. **257**, 133 (1995).
[69] J. H. G. van Pol *et al.*, Phys. Rev. Lett. **76**, 1425 (1996).
[70] S. Kox *et al.*, Phys. Rev. C **35**, 1678 (1987).
[71] P. Désesquelles *et al.*, Phys. Rev. C **48**, 1828 (1993).
[72] L. Beaulieu, Ph.D. thesis, Université Laval, 1996.
[73] P. Pawlowski *et al.*, Phys. Rev. C **54**, R10 (1996).
[74] L. Beaulieu *et al.*, Phys. Rev. C **54**, R973 (1996).
[75] A. Schüttauf *et al.*, Nucl. Phys. **A607**, 457 (1996).
[76] A. S. Botvina *et al.*, Nucl. Phys. **A592**, 257 (1995).
[77] K. Hagel *et al.*, Phys. Rev. C **50**, 2017 (1994).